Complex Frequency Shifted Perfectly Matched Layer Boundary Conditions for Frequency-Domain Elastic Wavefield Simulations

ZHENCONG ZHAO,[1] JINGYI CHEN,[1] MINGHUA XU,[2] and XIAOBO LIU[1]

Abstract—To absorb unwanted seismic reflections caused by the truncated boundaries, various absorbing boundary conditions have been developed for seismic numerical modeling in both time and frequency domains. Among the various types of perfectly matched layer (PML) boundary conditions, complex frequency shifted PML (CFS-PML) has attracted much attention in time-domain wavefield simulations because it can better handle evanescent and grazing waves. In this paper, we extend the CFS-PML boundary condition to frequency-domain finite-difference seismic modeling, which has several advantages over time-domain modeling including the convenient implementation of multiple sources and a straightforward extension of adding attenuation factors. A comparison with an analytical solution is used to investigate the validity of the proposed CFS-PML algorithm. CFS-PML shows better absorbing behavior than the classical PML boundary condition in our model tests. We further implement CFS-PML for seismic wavefield simulations in an elongated elastic model and a complex model (Marmousi-II) with a free surface boundary condition.

Key words: Frequency-domain, finite-difference, elastic wave, CFS-PML, boundary conditions, free surface.

1. Introduction

To simulate seismic wave propagation in unbounded media, numerous absorbing boundary conditions have been applied to suppress the artificial reflections caused by truncated boundaries, such as the Clayton boundary condition (Clayton and Engquist 1977), sponge boundary conditions (Cerjan et al. 1985; Shin 1995), the Higdon boundary conditions (Higdon 1986, 1987) and the hybrid boundary condition (Liu and Sen 2012). These boundary conditions have been used for seismic modeling in the time domain (Clayton and Engquist 1977; Peng and Toksöz 1995; Gao et al. 2015) as well as in the frequency domain (Pratt 1990; Pratt and Worthington 1990; Shin 1995; Ren and Liu 2013). Unfortunately, most of these boundary conditions are not effective for greater incidence angles (Tsynkov 1998).

Berenger (1994) introduced the perfectly matched layer (PML) absorbing boundary condition for electromagnetic wave simulations, which has provided better absorbing performance compared with the above mentioned absorbing boundary conditions. The implementation of the PML boundary condition is based on a complex coordinate stretching along the coordinates in the frequency domain. Collino and Tsogka (2001) applied the PML to seismic wavefield simulation in the time domain. Soon after, the PML boundary condition was extended to seismic numerical modeling in the frequency domain (Operto et al. 2007; Liao et al. 2009; Li et al. 2015; Zhao et al. 2017). Although the PML boundary condition has the advantage of absorbing the evanescent field in discrete space, it suffers from spurious reflections at grazing incidence (Komatitsch and Martin, 2007) and exponential instabilities in lengthy simulations of elastic models with free surface boundary conditions (Meza-Fajardo and Papageorgiou, 2008; Zeng et al. 2011) and in anisotropic media cases (Bécache et al. 2004; Komatitsch and Martin, 2007; Meza-Fajardo and Papageorgiou, 2008).

The complex frequency shifted perfectly matched layer (CFS-PML) boundary condition was proposed for electromagnetic media by Roden and Gedney (2000) and was introduced to elastodynamics by Festa et al. (2005). It has been proven to offer

[1] Seismic Anisotropy Group, Department of Geosciences, The University of Tulsa, 800 South Tucker Drive, Tulsa, OK 74104, USA. E-mail: jingyi-chen@utulsa.edu
[2] CCDC Geological Exploration & Development Research Institute, Chengdu 610041, Sichuan, China.

effective absorption of evanescent and grazing waves in time-domain seismic modeling (Komatitsch and Martin 2007; Martin et al. 2008; Chen et al. 2014; Gvozdic and Djurdjevic 2017). However, to our knowledge, we have not seen any implementation of the CFS-PML boundary condition in a frequency-domain seismic wavefield simulation. Seismic wavefield simulations in the frequency domain have several advantages over time-domain modeling, including the easy implementation of multiple sources and the straightforward extension of adding attenuation factors (Marfurt and Shin 1989; Jo et al. 1996; Operto et al. 2009; Moreira et al. 2014).

The numerical techniques for simulating seismic wave propagation in the frequency domain include the finite element method (Marfurt 1984; Zhao et al. 2017) and the finite-difference method (Moreira et al. 2014; Doyon and Giroux 2014). The finite-difference method is the most popular numerical method due to its simple implementation and good balance between accuracy and efficiency.

In this paper, we propose to apply the CFS-PML absorbing boundary condition to the frequency-domain finite-difference elastic wavefield simulation. During the implementation, we use the Intel Pardiso Solver to solve the large sparse matrix (Liu et al. 2017). Numerical examples show that the CFS-PML boundary condition works better than the classical PML boundary condition. We also investigate the performance of the CFS-PML boundary condition with the existence of a free surface boundary condition. The tests show that our algorithm can successfully simulate the wave propagation, and the CFS-PML boundary condition can efficiently absorb the Rayleigh waves as well.

2. Governing Equations

The 2D frequency-domain wave equations in elastic isotropic media are given by (Pratt 1990):

$$\rho\omega^2 u + \frac{\partial}{\partial x}\left[\lambda\left(\frac{\partial u}{\partial x} + \frac{\partial v}{\partial z}\right) + 2\mu\frac{\partial u}{\partial x}\right]$$
$$+ \frac{\partial}{\partial z}\left[\mu\left(\frac{\partial v}{\partial x} + \frac{\partial u}{\partial z}\right)\right] + f$$
$$= 0 \tag{1a}$$

$$\rho\omega^2 v + \frac{\partial}{\partial z}\left[\lambda\left(\frac{\partial u}{\partial x} + \frac{\partial v}{\partial z}\right) + 2\mu\frac{\partial v}{\partial z}\right]$$
$$+ \frac{\partial}{\partial x}\left[\mu\left(\frac{\partial v}{\partial x} + \frac{\partial u}{\partial z}\right)\right] + g$$
$$= 0 \tag{1b}$$

where u and v are temporal Fourier components of the horizontal and vertical displacements, respectively; f and g are Fourier components of the horizontal and vertical body forces; ρ is the bulk density; λ and μ are the Lamé parameters, and ω is the angular frequency.

The discretized forms of Eq. (1) can be expressed as:

$$\omega^2\rho_{i,j}u_{i,j} + \frac{1}{\Delta x^2}\left[u_{i+1,j}(\lambda+2\mu)_{i+1,j} - 2u_{i,j}(\lambda+2\mu)_{i,j}\right.$$
$$+ u_{i-1,j}(\lambda+2\mu)_{i-1,j}\Big]$$
$$+ \frac{1}{4\Delta x\Delta z}\left[\lambda_{i+1,j}(v_{i+1,j+1} - v_{i+1,j-1})\right.$$
$$- \lambda_{i-1,j}(v_{i-1,j+1} - v_{i-1,j-1})\Big]$$
$$+ \frac{1}{4\Delta x\Delta z}\left[\mu_{i,j+1}(v_{i+1,j+1} - v_{i-1,j+1})\right.$$
$$- \mu_{i,j-1}(v_{i+1,j-1} - v_{i-1,j-1})\Big]$$
$$+ \frac{1}{\Delta z^2}\left[u_{i,j+1}\mu_{i,j+1} - 2u_{i,j}\mu_{i,j} + u_{i,j-1}\mu_{i,j-1}\right] + f_{i,j} = 0 \tag{2}$$

and

$$\omega^2\rho_{i,j}v_{i,j} + \frac{1}{\Delta z^2}\left[v_{i,j+1}(\lambda+2\mu)_{i,j+1} - 2v_{i,j}(\lambda+2\mu)_{i,j}\right.$$
$$+ v_{i,j-1}(\lambda+2\mu)_{i,j-1}\Big]$$
$$+ \frac{1}{4\Delta x\Delta z}\left[\lambda_{i,j+1}(u_{i+1,j+1} - u_{i-1,j+1})\right.$$
$$- \lambda_{i,j-1}(u_{i+1,j-1} - u_{i-1,j-1})\Big]$$
$$+ \frac{1}{4\Delta x\Delta z}\left[\mu_{i+1,j}(u_{i+1,j+1} - u_{i+1,j-1})\right.$$
$$- \mu_{i-1,j}(u_{i-1,j+1} - u_{i-1,j-1})\Big]$$
$$\frac{1}{\Delta x^2}\left[v_{i+1,j}\mu_{i+1,j} - 2v_{i,j}\mu_{i,j} + v_{i-1,j}\mu_{i-1,j}\right] + g_{i,j} = 0 \tag{3}$$

where Δx and Δz are the grid sizes in the horizontal and vertical directions, respectively.

As introduced in Pratt (1990), the second-order finite-difference star can be expressed as:

$$
\begin{matrix}
M_1 & M_4 & M_7 \\
M_2 & M_5 & M_8 \\
M_3 & M_6 & M_9.
\end{matrix}
$$

The elements of the star for the interior region can be directly obtained by collecting the terms at each grid point in Eqs. (2) and (3):

$$
M_1 = \frac{\lambda_{i-1,j} + \mu_{i-1,j}}{4\Delta x \Delta z} \begin{bmatrix} 0 & 1 \\ 1 & 0 \end{bmatrix} \tag{4}
$$

$$
M_2 = \frac{1}{(\Delta z)^2} \begin{bmatrix} \mu_{i,j-1} & 0 \\ 0 & (\lambda + 2\mu)_{i,j-1} \end{bmatrix} \tag{5}
$$

$$
M_3 = -\begin{bmatrix} 0 & \frac{\lambda_{i-1,j} + \mu_{i-1,j}}{4\Delta x \Delta z} \\ \frac{\lambda_{i,j+1} + \mu_{i,j+1}}{4\Delta x \Delta z} & 0 \end{bmatrix} \tag{6}
$$

$$
M_4 = \frac{1}{(\Delta z)^2} \begin{bmatrix} \mu_{i-1,j} & 0 \\ 0 & (\lambda + 2\mu)_{i,j-1} \end{bmatrix} \tag{7}
$$

$$
M_5 = \begin{bmatrix} \omega_{i,j}^2 \rho_{i,j} - \frac{2}{(\Delta x)^2}(\lambda_{i,j} + 2\mu_{i,j}) & 0 \\ 0 & \omega_{i,j}^2 \rho_{i,j} - \frac{2}{(\Delta x)^2}(\lambda_{i,j} + 2\mu_{i,j}) \end{bmatrix} \tag{8}
$$

$$
M_6 = \frac{1}{(\Delta z)^2} \begin{bmatrix} \mu_{i,j+1} & 0 \\ 0 & \lambda_{i,j+1} + 2\mu_{i,j+1} \end{bmatrix} \tag{9}
$$

$$
M_7 = -\frac{1}{4\Delta x \Delta z} \begin{bmatrix} 0 & \lambda_{i+1,j} + \mu_{i,j-1} \\ \lambda_{i,j-1} + \mu_{i+1,j} & 0 \end{bmatrix} \tag{10}
$$

$$
M_8 = \frac{1}{(\Delta x)^2} \begin{bmatrix} (\lambda + 2\mu)_{i+1,j} & 0 \\ 0 & \mu_{i+1,j} \end{bmatrix} \tag{11}
$$

$$
M_9 = \frac{1}{4\Delta x \Delta z} \begin{bmatrix} 0 & \mu_{i,j+1} + \lambda_{i+1,j} \\ \mu_{i+1,j} + \lambda_{i,j+1} & 0 \end{bmatrix} \tag{12}
$$

3. Boundary Conditions

3.1. Perfectly Matched Layer (PML) Boundary Condition

The main idea of the PML is to introduce a complex coordinate stretching system in the horizontal and vertical directions. For example, the new horizontal coordinate $\tilde{x}$ is expressed as:

$$
\tilde{x}(x) = x - \frac{i}{\omega} \int_0^x d_x(s) ds \tag{13}
$$

which, upon differentiation, can be written as:

$$
\frac{\partial}{\partial \tilde{x}} = \frac{i\omega}{i\omega + d_x(x)} \frac{\partial}{\partial x} = \frac{1}{e_x} \frac{\partial}{\partial x} \tag{14}
$$

where the stretching coefficient $e_x = 1 - i\frac{d_x(x)}{\omega}$ and the damping factor $d_x(x)$ linearly changes with x within the PML ranging from 0 to a positive value. Here, we use

$$
d_x(x) = 2\pi a_0 f_0 \left(\frac{x_i}{L_{PML}}\right)^2 \tag{15}
$$

where x_i is the distance from the inner PML boundary in the horizontal direction, a_0 is the optimized parameter, which is normally referred to 1.79 (Zeng et al. 2001), f_0 is the dominant frequency and L_{PML} is the thickness of the PML boundary. The choice of a_0 is obtained by using a trial and error approach depending on the thickness of PML boundary. The optimal a_0 is the one to make the minimum energy of reflections coming from the edges (Hustedt et al. 2004). In our numerical tests, the best value of a_0 is 0.6 for a thickness of 40 grids. The new vertical stretching coordinate has a form that is similar to the new horizontal coordinate.

By using the complex coordinate stretching method, the implementation of the PML boundary condition to the frequency-domain seismic wave equations can be expressed as (Yuan et al. 2014):

$$
\frac{1}{e_x}\frac{\partial}{\partial x}\left[(\lambda+2\mu)\frac{1}{e_x}\frac{\partial u}{\partial x}\right] + \frac{1}{e_z}\frac{\partial}{\partial z}\left[\mu\frac{1}{e_z}\frac{\partial u}{\partial z}\right] + \frac{1}{e_x}\frac{\partial}{\partial x}\left(\lambda\frac{1}{e_z}\frac{\partial v}{\partial z}\right)
$$
$$
+ \frac{1}{e_z}\frac{\partial}{\partial z}\left(\mu\frac{1}{e_x}\frac{\partial v}{\partial x}\right) + \rho\omega^2 u + f = 0 \tag{16}
$$

$$
\frac{1}{e_z}\frac{\partial}{\partial z}\left[(\lambda+2\mu)\frac{1}{e_z}\frac{\partial v}{\partial z}\right] + \frac{1}{e_x}\frac{\partial}{\partial x}\left[\mu\frac{1}{e_x}\frac{\partial v}{\partial x}\right] + \frac{1}{e_z}\frac{\partial}{\partial z}\left(\lambda\frac{1}{e_x}\frac{\partial u}{\partial x}\right)
$$
$$
+ \frac{1}{e_x}\frac{\partial}{\partial x}\left(\mu\frac{1}{e_z}\frac{\partial u}{\partial z}\right) + \rho\omega^2 v + g = 0 \tag{17}
$$

3.2. Complex Frequency Shifted Perfectly Matched Layer (CFS-PML) Boundary Condition

With the CFS-PML boundary condition, seismic wave equations can also be expressed as Eqs. (16)
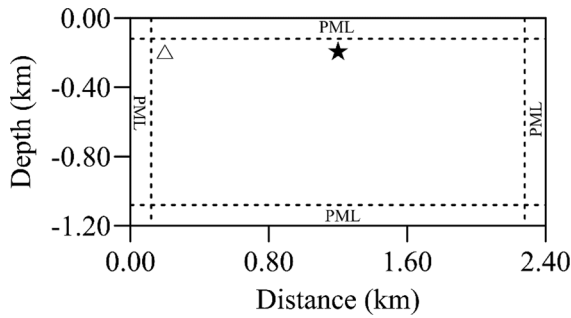
Figure 1
Sketch of the elongated elastic model. The dashed lines are the inner boundaries of the PML and CFS-PML. The star and triangle represent the source and receiver, respectively

and (17). However, the stretching coefficients along the horizontal and vertical coordinates are:

$$e(x) = k(x) + \frac{d_x(x)}{\alpha(x) + i\omega} \tag{18}$$

and

$$e(z) = k(z) + \frac{d_z(z)}{\alpha(z) + i\omega} \tag{19}$$

As an example, the damping factor $d_x(x)$ along the horizontal direction can be described as follows:

$$d_x(x) = d_0 \left(\frac{x}{L_{PML}} \right)^{P_d} \tag{20}$$

And, two other variables $k(x)$ and $\alpha(x)$ are expressed as:

$$k(x) = 1 + (k_{max} - 1) \left(\frac{x}{L_{PML}} \right)^{P_k} \tag{21}$$

and

$$\alpha(x) = \alpha_{max} \left(1 - \left(\frac{x}{L_{PML}} \right) \right) \tag{22}$$

where $\alpha_{max} = \pi f_0$ (Komatitsch and Martin 2007), f_0 is the dominant frequency of the source, L_{PML} is the thickness of the CFS-PML boundary, x is the distance to the inner CFS-PML boundary and d_0 can be written as (Collino and Tsogka 2001):

$$d_0 = -\frac{(P_d + 1) \times V_p^{max} \times \log(Rcoef)}{2 \times L_{PML}} \tag{23}$$

Here, V_p^{max} is the maximum P-wave velocity and $Rcoef$ is the objective reflectivity (0.001% used in this paper). The parameters P_d and P_k range from 1 to 4, and 2 is commonly used (Taflove 1998). In our paper, P_d and P_k are assumed to be 2 and the optimal k_{max} is 1 after numerical tests for the 40-grid thickness of the CFS-PML boundary condition. One can observe that in the particular case of $k_{max} = 1$ and $\alpha_{max} = 0.0$, the CFS-PML boundary condition degenerates to the classical PML boundary condition.

3.3. Free Surface Boundary Condition

To model seismic wave propagation in an elastic model with a realistic surface (air/solid interface), we
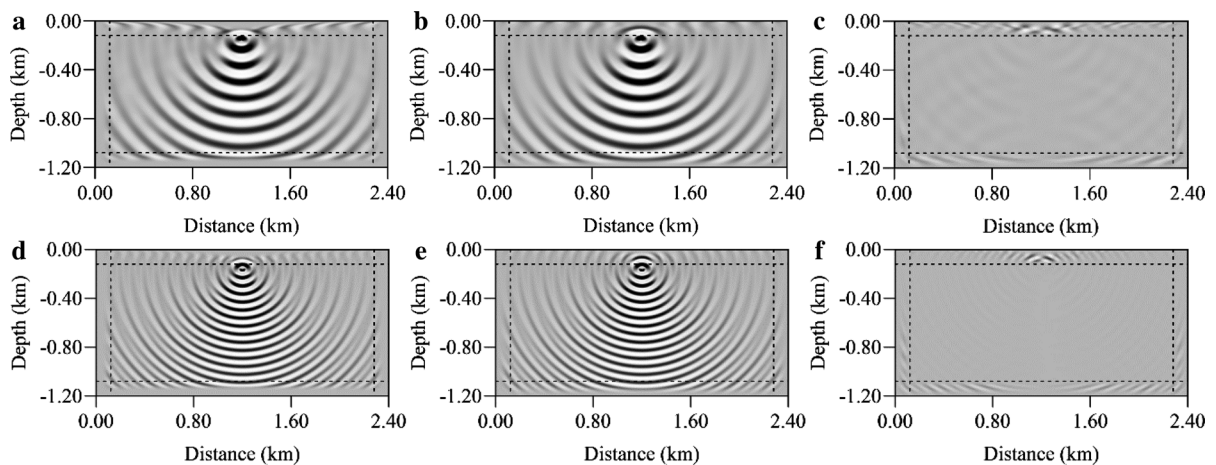

Figure 2
The 15.1 Hz (top panel) and 30.1 Hz (lower panel) real-part solutions of the elastic wavefields in the horizontal plane using the PML (**a**, **d**) and CFS-PML (**b**, **e**) absorbing boundary conditions and the differences between the two methods (**c**, **f**)
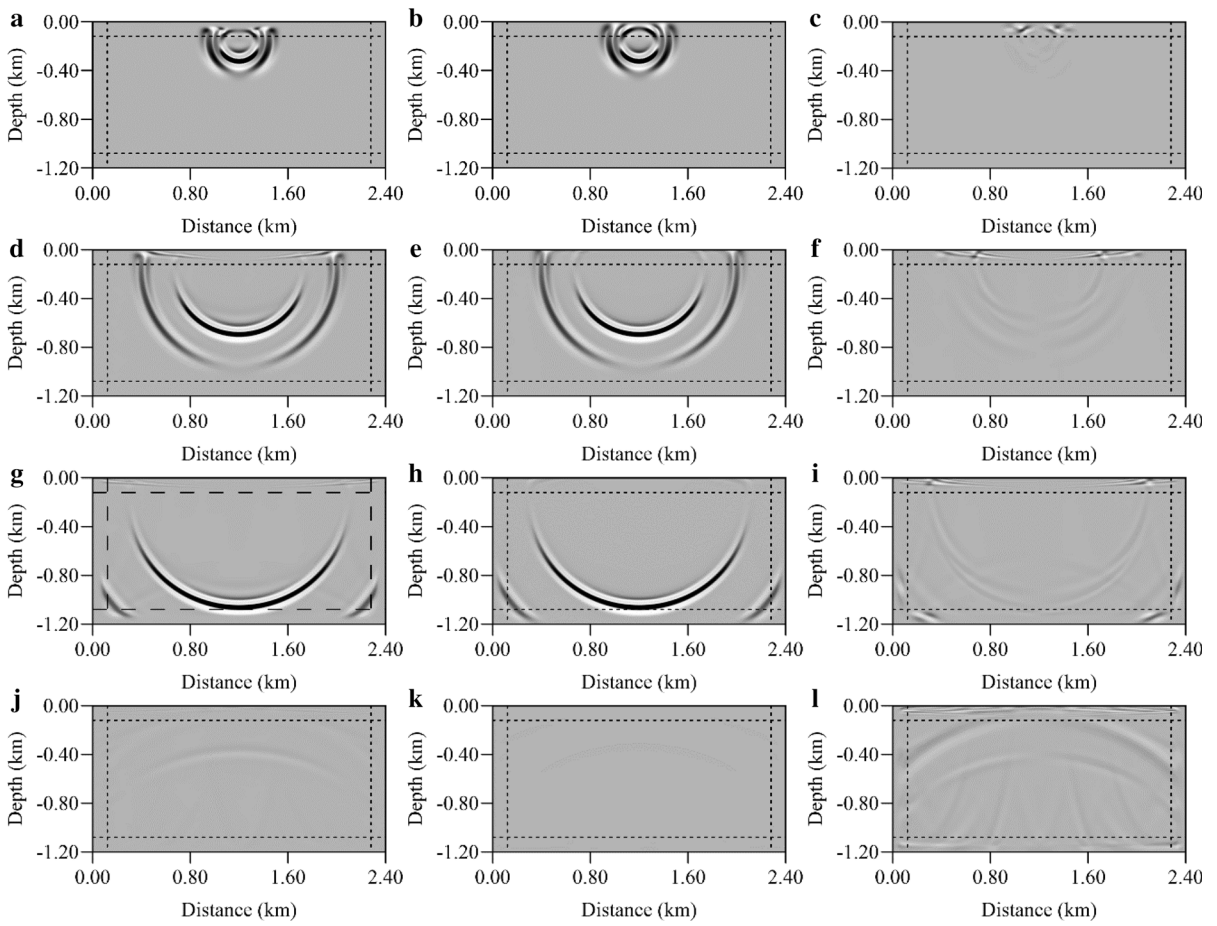
Figure 3
Snapshots of the displacement in the horizontal plane using the PML (**a**, **d**, **g**, **j**), CFS-PML boundary condition (**b**, **d**, **f**, **h**) and the differences between these two methods (**c**, **f**, **i**, **l**) at 0.1792 s, 0.3656 s, 0.5520 s and 0.9247 s. The dashed lines are the inner boundaries of the PML and CFS-PML boundary conditions

apply the traction free surface boundary condition to the surface of the model (Lan and Zhang, 2011), which can be expressed as:

$$\frac{\partial u}{\partial z} + \frac{\partial v}{\partial x} = 0 \qquad (24)$$

and

$$\gamma \frac{\partial u}{\partial x} + \frac{\partial v}{\partial z} = 0 \qquad (25)$$

where $\gamma = \left(1 - \frac{2V_s^2}{V_p^2}\right)$. V_p and V_s are seismic P- and S-wave velocities.

In the implementation of the free surface boundary condition, an extra row is added above the actual free surface. In addition, the complex coordinate stretching method is also applied to the free surface boundary condition at the left and right boundaries of the free surface.

4. Source Implementation

The Ricker wavelet used as a source signature in the frequency domain can be expressed as (Wang 2015):

$$S(\omega) = \frac{2}{\sqrt{\pi}} \frac{\omega^2}{\omega_p^3} \exp\left[-\left(\frac{\omega}{\omega_p}\right)^2\right] \qquad (26)$$
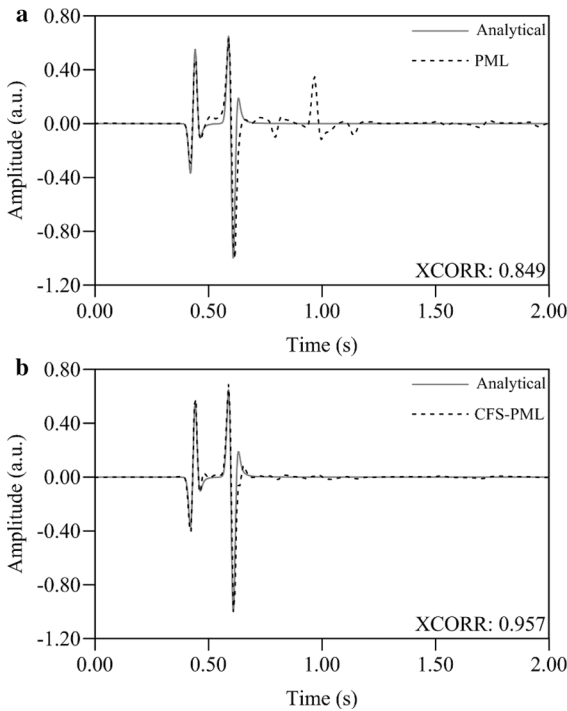
a

b

Figure 4
Comparison between an analytical solution and seismograms of the horizontal component for the receiver at the grid (50, 50) using the PML (**a**) and CFS-PML (**b**) boundary conditions, respectively
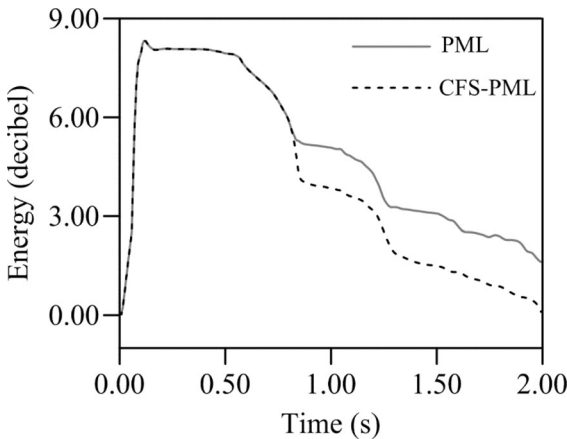

Figure 5
Wavefield energy decay curves using the PML (solid gray line) and CFS-PML (dashed dark line) boundary conditions for the elongated elastic model

where ω_p is the angular peak frequency and ω is the angular frequency.

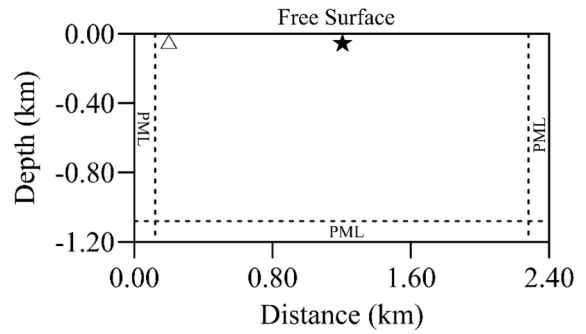According to Yin et al. (2006), the point source can be expressed as:

Figure 6
Sketch of the elongated elastic model with a free surface boundary condition. The dashed lines denote the inner boundaries of the PML and CFS-PML boundary conditions. The star and triangle represent the source and receiver, respectively. The free surface boundary condition is used at the surface

$$\begin{bmatrix} f \\ g \end{bmatrix} = \begin{bmatrix} \delta \cdot S_u(\omega) \\ \delta \cdot S_v(\omega) \end{bmatrix} \qquad (27)$$

where $\delta = \begin{cases} 1, & (x_0, y_0) \\ 0, & otherwise \end{cases}$.

Here, f and g are Fourier components of the horizontal and vertical body forces in the frequency domain; the source is located at grid point (x_0, y_0); $S_u(\omega)$ and $S_v(\omega)$ are the horizontal and vertical components of the source signature. The vertical force source is used in the following model tests.

5. Numerical Experiments

To test the validity and performance of the CFS-PML absorbing boundary in frequency-domain finite-difference seismic modeling, we examine three elastic models in this section: an elongated model, an elongated model with a free surface boundary condition and the Marmousi-II model with a free surface boundary condition.

5.1. Elongated Elastic Model

The elongated elastic model (Fig. 1) is discretized by 600×300 grid points with a grid spacing of 4 m, which has a size of 2.4 km $\times$ 1.2 km. The P- and S-wave velocities and density are 3000 m/s, 2000 m/s and 2000 m/s, respectively. The thickness of the PML boundary is 120 m (30 grids). We use the same thickness for the CFS-PML boundary. The frequency
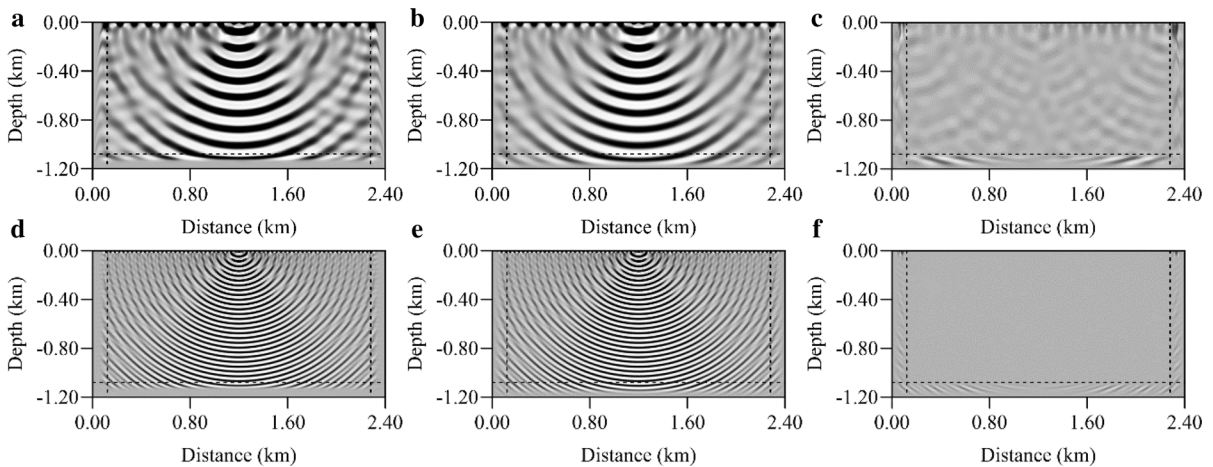
Figure 7
The 15.1 Hz (top panel) and 30.1 Hz (lower panel) real-part solutions of the elastic wavefields in the horizontal plane using the PML (**a**, **d**) and CFS-PML (**b**, **e**) absorbing boundary conditions and the differences between these two methods (**c**, **f**)

range is from 0.1 to 79.6 Hz with an increment of 0.5 Hz. The source (star) described by a Ricker wavelet with the peak frequency of 20 Hz and delay of 0.1 s is located at grid point (300, 40) as a horizontal source. A receiver (triangle) is located at grid point (50, 50), which is used to test the absorbing performance of the CFS-PML at grazing incidence angles. In Fig. 1, the dashed lines represent the inner boundaries of the PML and CFS-PML

Figure 2 shows the 15.1 Hz (top panel) and 30.1 Hz (bottom panel) real-part solutions of the horizontal component of the elastic wavefields using the PML and CFS-PML boundary conditions. Observe that distinct artificial reflections are found in the wavefields using the PML (a, d). CFS-PML boundary condition offers the better suppression of the artificial reflections in the wavefields (b, e). Also, the differences (c, f) between the real-part solutions calculated with PML and CFS-PML boundary conditions are large.

Figure 3 shows snapshots of the displacement in the horizontal plane calculated with PML (left panel) and CFS-PML (right panel) at 0.1792 s, 0.3656 s, 0.5520 s and 0.9247 s. One can easily observe spurious reflections from the snapshots calculated with the PML boundary condition after P- and S-waves reach the boundaries (a, d, g, j). However, we

do not observe the distinct artificial reflections from the snapshots calculated with the CFS-PML boundary condition (b, e, h, k). Obvious differences between the snapshots calculated with PML and CFS-PML boundary conditions are observed in Fig. 3c, f, i, l. Figure 4 shows the comparison of horizontal component seismograms calculated using the PML and CFS-PML boundary conditions with an analytical solution (Aki and Richards 2002) for the receiver at grid point (50, 50). We find that the CFS-PML boundary condition (4b) provides better agreement with the analytical solution than the PML boundary condition (4a). The cross-correlation parameter XCORR between the analytical solution and the seismogram calculated is 0.849 with PML, whereas it is 0.957 with CFS-PML. The obvious improvement in the absorbing performance of the CFS-PML boundary condition can be observed.

We use the wavefield energy decay curve (Fig. 5) to further investigate the absorbing performance of the CFS-PML boundary condition. The wavefield energy is simply calculated as the square of the horizontal displacement within the simulation period (2 s). After the P-wave reaches the top boundary (0.113 s), the energy is gradually absorbed by the absorbing boundaries. We observe that the energy curve calculated with the CFS-PML has a faster
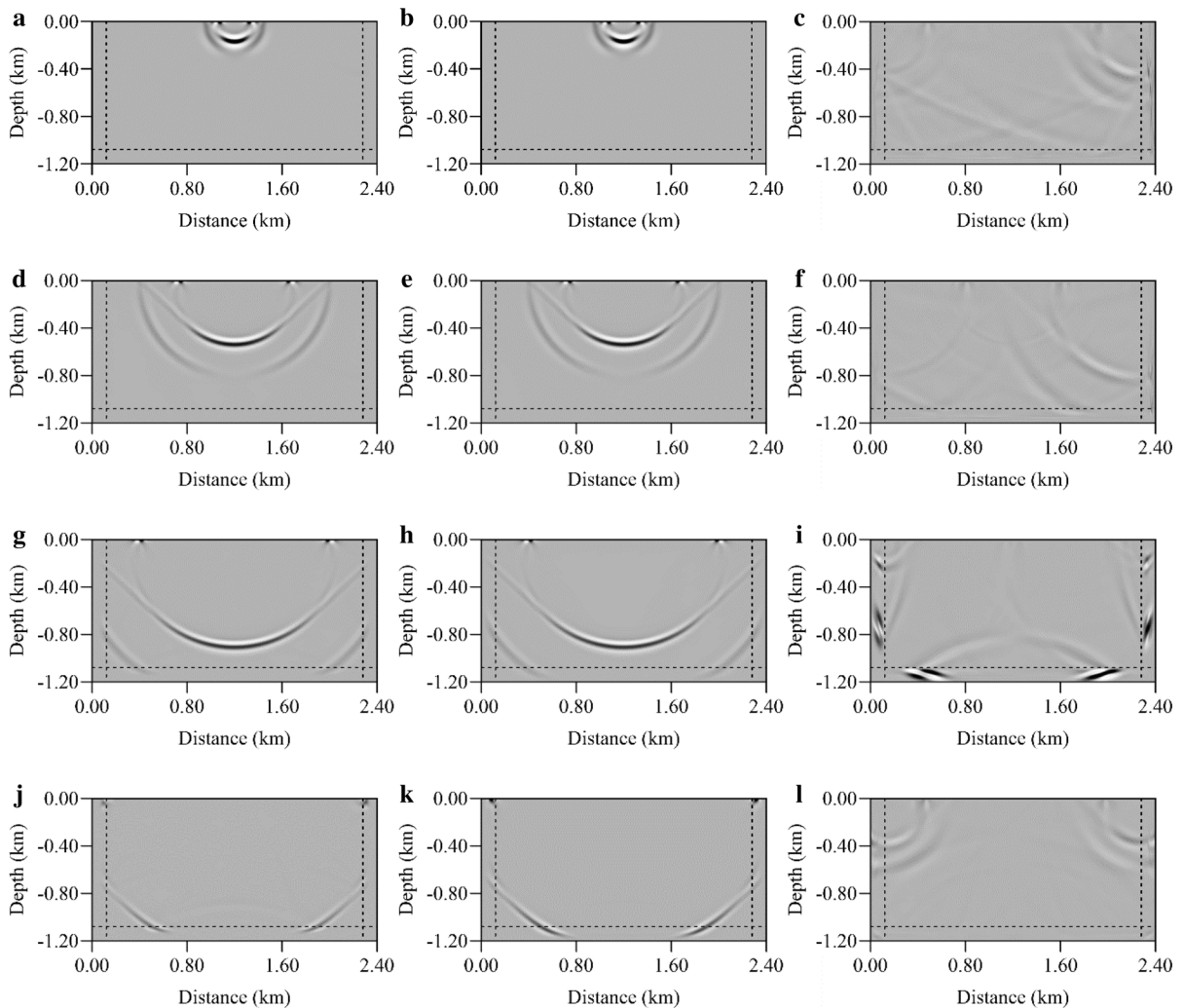
Figure 8

Snapshots of the displacement in the horizontal plane calculated with the PML (**a**, **d**, **g**, **j**), CPML boundary condition (**b**, **e**, **h**, **k**) and the differences between these two methods (**c**, **f**, **i**, **l**) at 0.179 s, 0.366 s, 0.552 s and 0.925 s. The dashed lines are the inner boundaries of the PML and CFS-PML boundary conditions

absorption than that calculated with the PML boundary condition, which indicates that the CFS-PML boundary condition performs better suppression of the artificial reflections than the PML boundary condition.

5.2. Elongated Elastic Model with a Free Surface

To further investigate the absorbing performance of the CFS-PML boundary condition with the existence of a free surface boundary condition, we built

an elongated elastic model with a free surface (Fig. 6). The absorbing boundary conditions are implemented to the left, right and bottom boundaries of the model, while the free surface boundary condition (Lan and Zhang 2011) is only applied at the surface. The star denotes the horizontal source located at grid point (300, 2), which is a Ricker wavelet with dominant frequency of 20 Hz and delay time of 0.1 s, and the triangle denotes a receiver located at grid point (60, 2). We chose the same
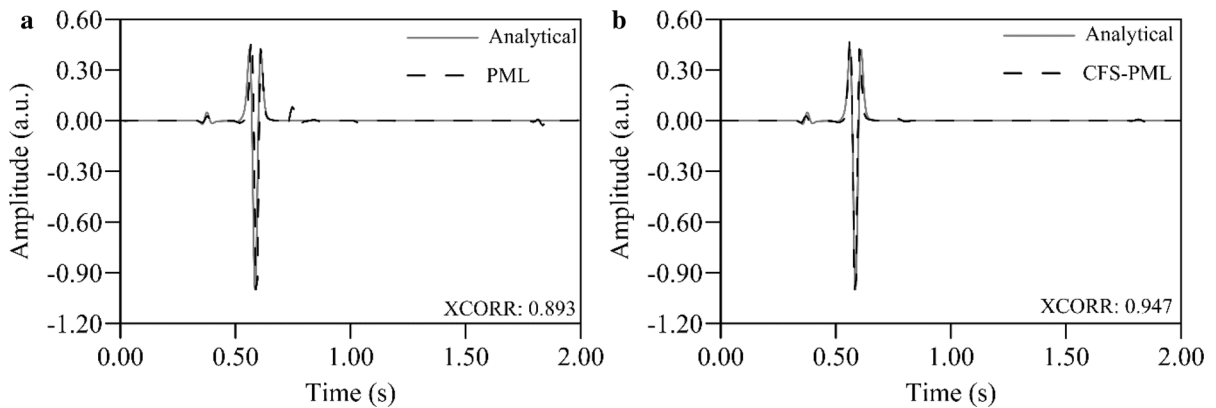
Figure 9
Comparison between an analytical solution and seismograms of the horizontal component for the receiver at grid (60, 2) using the PML (**a**) and CFS-PML (**b**) boundary conditions, respectively
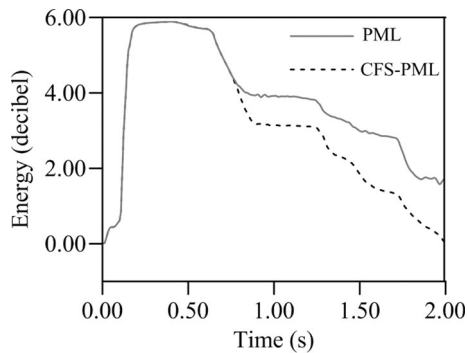

Figure 10
Wavefield energy decay curves using the PML (solid gray line) and CFS-PML (dashed dark line) boundary conditions for the elongated elastic model with a free surface boundary condition

values of the model parameters used in the last elongated elastic model.

Figure 7 shows the 15.1 Hz (top panel) and 30.1 Hz (bottom panel) real-part solutions of the horizontal component of the elastic wavefields using the PML and CFS-PML absorbing boundary conditions. One can observe the distinct spurious reflections in the wavefields using the PML boundary condition (a and d). As discussed before, we do not observe distinct artificial reflections in the wavefields using the CFS-PML boundary condition (b and e). In addition, we observe the Rayleigh wave at the surface.

Figure 8 shows snapshots of the displacement in the horizontal plane at 0.179 s, 0.366 s, 0.552 s and 0.925 s using the PML and CFS-PML absorbing

boundary conditions. One can easily observe serious spurious reflections from the snapshots calculated with the PML boundary condition (a, d, g and j). The CFS-PML boundary condition (b, e, h and k) works better than the PML boundary condition. The differences between snapshots calculated with PML and CFS-PML boundary conditions are shown in Fig. 8c, f, i, l.In addition, we can correctly simulate Rayleigh wave propagation at the surface.

Figure 9 shows the seismograms of the horizontal component for the receiver at the grid point (60, 2). The cross-correlation parameters XCORR between the analytical solution and the seismograms calculated with the PML and CFS-PML are 0.893 and 0.947, respectively. One can easily observe the artificial reflections in the seismogram calculated with the PML boundary condition. No distinct artificial reflections can be observed in the seismogram calculated with the CFS-PML boundary condition.

As in the previous study, the wavefield energy decay curves are investigated in Fig. 10. One can easily get the same conclusion that the CFS-PML boundary condition absorbs the energy faster than the PML boundary condition.

5.3. Marmousi-II Model with a Free Surface

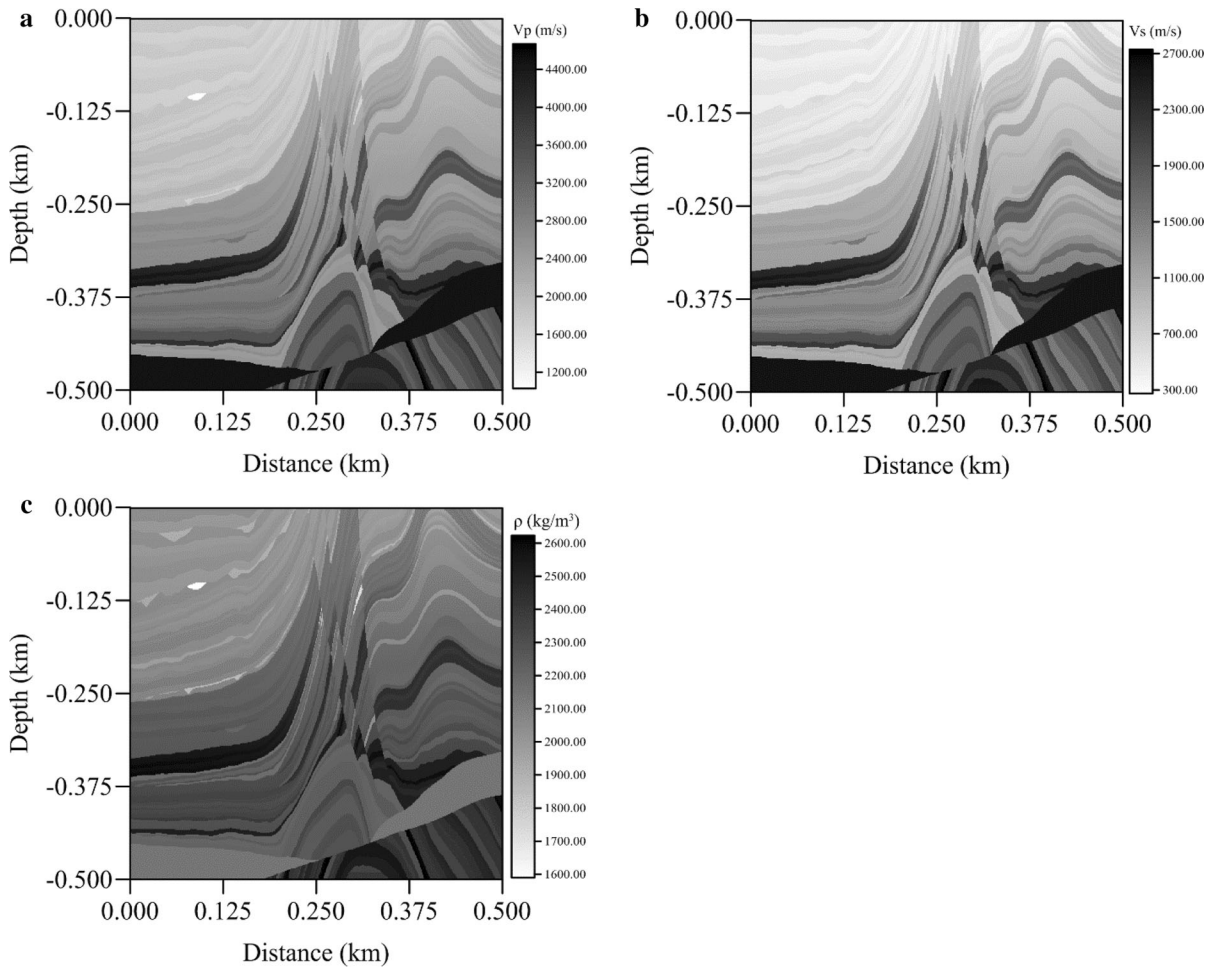To test the performance and validity of the proposed algorithm in the case of complex
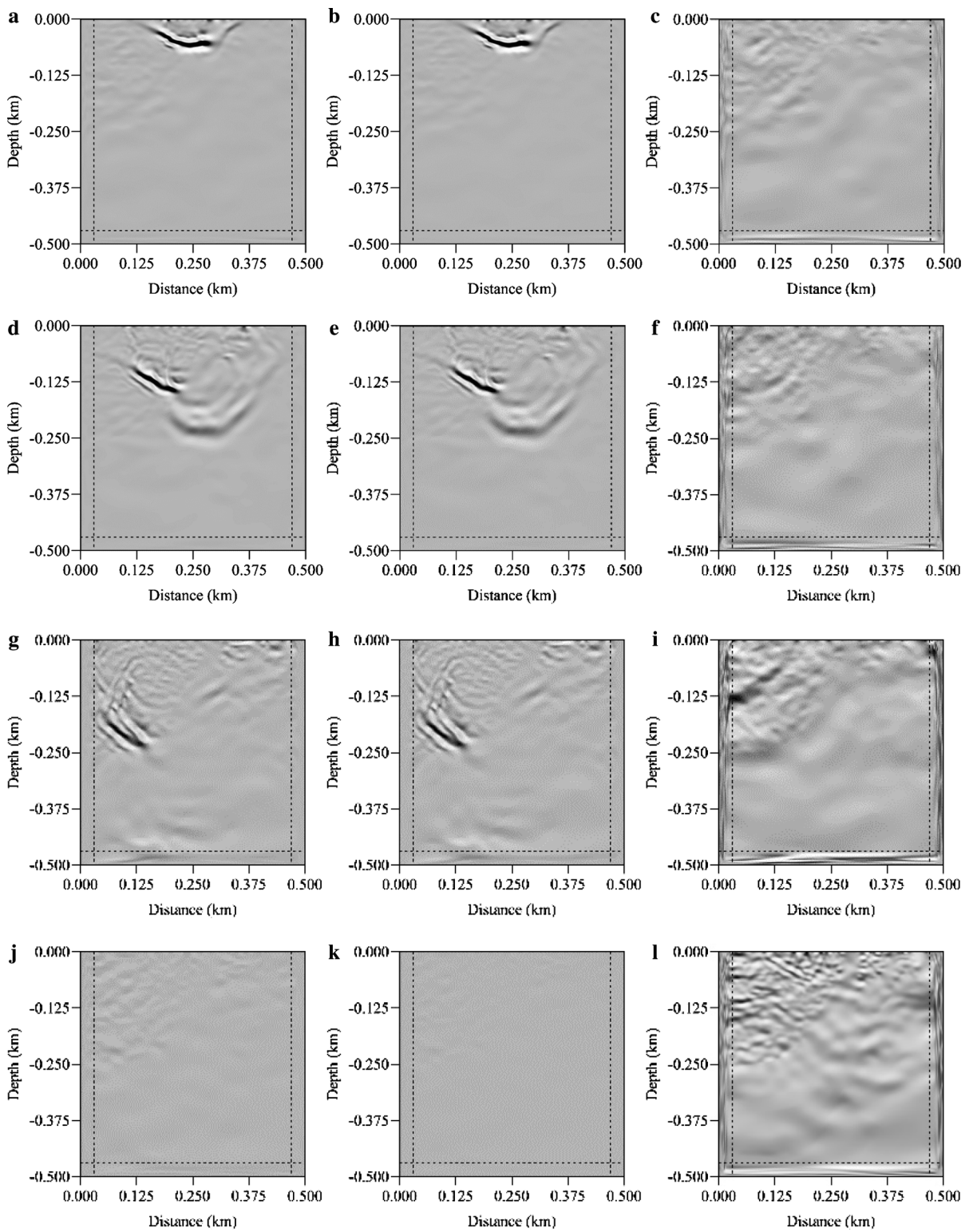
Figure 11
Sketch of Marmousi-II model including P-wave velocity (**a**), S-wave velocity (**b**) and density (**c**)

heterogeneous media, we simulated seismic wave propagation in the Marmousi-II model with a free surface. As shown in Fig. 11, the Marmousi-II model has a size of 500 m × 500 m, which is discretized by 500 × 500 grids with grid spacing of 1 m. A Ricker wavelet with the dominant frequency of 20 Hz and delay of 0.05 s was applied as horizontal source at grid point (240, 2). The frequency range is from 0.1 Hz to 69.6 Hz with an increment of 0.5 Hz. An array of receivers is located along grid points $j = 40$. The same PML and CFS-PML parameters were used in Sects. 5.1, 5.2.

Figure 12 shows snapshots of the horizontal displacement calculated with PML (left panel) and CFS-PML (right panel) at 0.1792 s, 0.3656 s, 0.5520 s and 0.9247 s. One can easily observe artificial reflections, after the P-, S- and surface waves reach the boundaries, in the snapshots calculated with the PML boundary condition. The CFS-PML boundary condition performs better absorption than the PML, and one cannot observe any obvious spurious reflections (b, e, h, k).

Figure 12   ▶
Snapshots of the displacement in the horizontal plane at 0.1792 s, 0.3656 s, 0.5520 s and 0.9247 s using the PML (**a**, **d**, **g**, **j**), CFS-PML (**b**, **e**, **h**, **k**) boundary conditions and the differences between these two methods (**c**, **f**, **i**, **l**). The dashed lines are the inner boundaries of both PML and CFS-PML boundary conditions
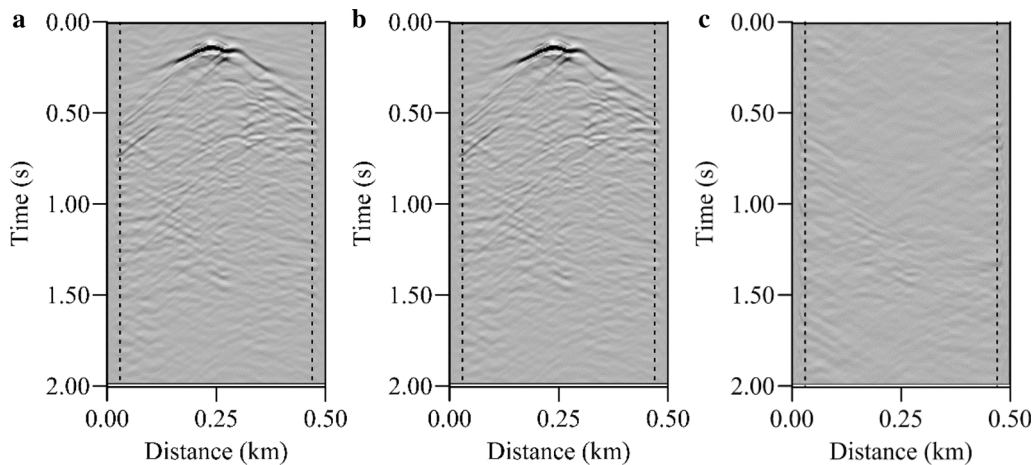
Figure 13
Shot gathers of Marmousi-II model calculated with PML (**a**) and CFS-PML (**b**) boundary conditions and the differences between these two methods (**c**)

Figure 13 shows the shot gathers of the horizontal displacements calculated with PML (a) and CFS-PML (b) boundary conditions. One can observe that the artificial reflections from the boundary conditions in the shot gather calculated with the PML boundary condition are stronger than those calculated with the CFS-PML boundary condition. Obvious differences can also be observed between the two shot gathers in Fig. 13c. One can observe obvious difference.

Here, we also use the wavefield energy decay curve to show the advantage of the CFS-PML over PML boundary condition (Fig. 14). One can observe that the energy calculated with the CFS-PML boundary condition is absorbed faster than the energy calculated with the PML boundary condition.

6. Conclusions

In this paper, we implemented the complex frequency shifted PML (CFS-PML) absorbing boundary condition in a frequency-domain finite-difference seismic wavefield simulation and compared its performance with the analytical solution. Numerical experiments show that the seismograms calculated with the CFS-PML boundary condition have a significant match with the analytical solution, and CFS-PML was found to be more efficient in absorbing artificial reflections than the PML boundary
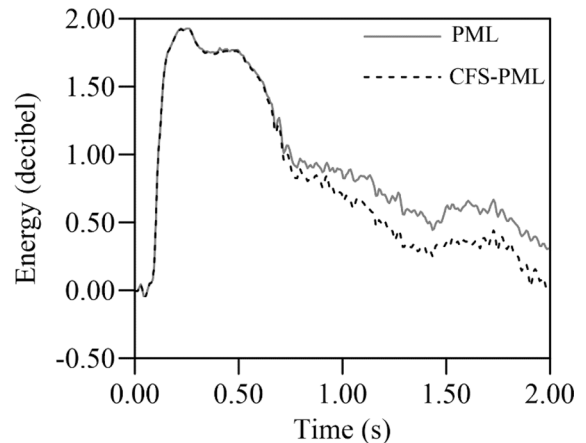

Figure 14
Wavefield energy decay curves using the PML (solid gray line) and CFS-PML (dashed dark line) boundary conditions for the Marmousi-II model with a free surface

condition. Seismic numerical modeling with CFS-PML will be extended to 3D elastic media in the future.

reviewers and associate editor Dr. Andrew Gorman for their constructive suggestions and comments, which significantly improved the quality of our manuscript.

Publisher's Note   Springer Nature remains neutral with regard to jurisdictional claims in published maps and institutional affiliations.

References

Aki, K., & Richards, P. G. (2002). *Quantitative seismology*. Mill Valley: University Science Books.

Bécache, E., Petropoulos, P. G., & Gedney, S. D. (2004). On the long-time behavior of unsplit perfectly matched layers. *IEEE Transactions on Antennas and Propagation, 52,* 1335–1342.

Berenger, J. P. (1994). A perfectly matched layer for the absorption of electromagnetic waves. *Journal of Computational Physics, 114,* 185–200.

Cerjan, C., Kosloff, D., Kosloff, R., & Reshef, M. (1985). A nonreflecting boundary condition for discrete acoustic and elastic wave equations. *Geophysics, 50,* 705–708.

Chen, H., Zhou, H., & Li, Y. (2014). Application of unsplit convolutional perfectly matched layer for scalar arbitrarily wide-angle wave equation. *Geophysics, 79,* 313–321.

Clayton, R., & Engquist, B. (1977). Absorbing boundary conditions for acoustic and elastic wave equations. *Bulletin of the Seismological Society of America, 67,* 1529–1540.

Collino, F., & Tsogka, C. (2001). Application of the perfectly matched absorbing layer model to the linear elastodynamic problem in anisotropic heterogeneous media. *Geophysics, 66,* 294–307.

Doyon, B. and Giroux, B., 2014. Practical aspects of 2.5D frequency-domain finite-difference modelling of viscoelastic waves: The SEG Technical Program Expanded Abstracts, 3482-3486.

Festa, G., Delavaud, E. and Vilotte, J.P., 2005. Interaction between surface waves and absorbing boundaries for wave propagation in geological basins: 2D numerical simulations: *Geophysical Research Letters, 32*.

Gao, Y., Song, H., Zhang, J., & Yao, Z. (2015). Comparison of artificial absorbing boundaries for acoustic wave equation modelling. *Exploration Geophysics, 48,* 76–93.

Gvozdic, B. D., & Djurdjevic, D. Z. (2017). Performance advantages of CPML over UPML absorbing boundary conditions in FDTD algorithm. *Journal of Electrical Engineering, 68,* 47–53.

Higdon, R. L. (1986). Absorbing boundary conditions for difference approximations to the multidimensional wave equation. *Mathematics of Computation, 47,* 437–459.

Higdon, R. L. (1987). Numerical absorbing boundary conditions for the wave equation. *Mathematics of Computation, 49,* 65–90.

Hustedt, B., Operto, S., & Virieux, J. (2004). Mixed-grid and staggered-grid finite-difference methods for frequency-domain acoustic wave modelling. *Geophysical Journal International, 157,* 1269–1296.

Jo, C. H., Shin, C., & Suh, J. H. (1996). An optimal 9-point, finite-difference, frequency-space, 2-D scalar wave extrapolator. *Geophysics, 61,* 529–537.

Komatitsch, D., & Martin, R. (2007). An unsplit convolutional perfectly matched layer improved at grazing incidence for the seismic wave equation. *Geophysics, 72,* 155–167.

Lan, H., & Zhang, Z. (2011). Comparative study of the free-surface boundary condition in two-dimensional finite-difference elastic wave field simulation. *Journal of Geophysics and Engineering, 8,* 275–286.

Li, Y., Métivier, L., Brossier, R., Han, B., & Virieux, J. (2015). 2D and 3D frequency-domain elastic wave modeling in complex media with a parallel iterative solver. *Geophysics, 80,* 101–118.

Liao, J., Wang, H., & Ma, Z. (2009). 2-D elastic wave modeling with frequency-space 25-point finite-difference operators. *Applied Geophysics, 6,* 259–266.

Liu, W., Lin, P., Lü, Q., Chen, R., Cai, H., & Li, J. (2017). Time domain and frequency domain induced polarization modeling for three-dimensional anisotropic medium. *Journal of Environmental and Engineering Geophysics, 22,* 435–439.

Liu, Y., & Sen, M. K. (2012). A hybrid absorbing boundary condition for elastic staggered-grid modelling. *Geophysical Prospecting, 60,* 1114–1132.

Marfurt, K. J. (1984). Accuracy of finite-difference and finite-element modeling of the scalar and elastic wave equations. *Geophysics, 49,* 533–549.

Marfurt, K. J., & Shin, C. S. (1989). The future of iterative modeling in geophysical exploration. *Handbook of geophysical exploration: Seismic Exploration*. Oxford: Elsevier.

Martin, R., Komatitsch, D., & Ezziani, A. (2008). An unsplit convolutional perfectly matched layer improved at grazing incidence for seismic wave propagation in poroelastic media. *Geophysics, 73,* 51–61.

Meza-Fajardo, K. C., & Papageorgiou, A. S. (2008). A nonconvolutional, split-field, perfectly matched layer for wave propagation in isotropic and anisotropic elastic media: stability analysis. *Bulletin of the Seismological Society of America, 98,* 1811–1836.

Moreira, R. M., Cetale Santos, M. A., Martins, J. L., Silva, D. L. F., Pessolani, R. B. V., Filho, D. M. S., et al. (2014). Frequency-domain acoustic-wave modeling with hybrid absorbing boundary conditions. *Geophysics, 79,* 39–44.

Operto, S., Virieux, J., Amestoy, P., L'Excellent, J. Y., Giraud, L., & Ali, H. B. H. (2007). 3D finite-difference frequency-domain modeling of visco-acoustic wave propagation using a massively parallel direct solver: A feasibility study. *Geophysics, 72,* 195–211.

Operto, S., Virieux, J., Ribodetti, A., & Anderson, J. E. (2009). Finite-difference frequency-domain modeling of viscoacoustic wave propagation in 2D tilted transversely isotropic (TTI) media. *Geophysics, 74,* 75–95.

Peng, C., & Toksöz, M. N. (1995). An optimal absorbing boundary condition for elastic wave modeling. *Geophysics, 60,* 296–301.

Pratt, R. G. (1990). Frequency-domain elastic wave modeling by finite differences: A tool for crosshole seismic imaging. *Geophysics, 55,* 626–632.

Pratt, R. G., & Worthington, M. H. (1990). Inverse theory applied to multi-source cross-hole tomography. Part 1: Acoustic wave-equation method. *Geophysical Prospecting, 38,* 287–310.

Ren, Z., & Liu, Y. (2013). A hybrid absorbing boundary condition for frequency-domain finite-difference modelling. *Journal of*

Geophysics and Engineering. https://doi.org/10.1088/1742-2132/10/5/054003.

Roden, J. A., & Gedney, S. D. (2000). Convolutional PML (CPML): An efficient FDTD implementation of the CFS-PML for arbitrary media. *Microwave and optical technology letters, 27,* 334–338.

Shin, C. (1995). Sponge boundary condition for frequency-domain modeling. *Geophysics, 60,* 1870–1874.

Taflove, A. (1998). *Advances in computational electrodynamics: the finite-difference time-domain method*. Boston: Artech House.

Tsynkov, S. V. (1998). Numerical solution of problems on unbounded domains. A review. *Applied Numerical Mathematics, 27,* 465–532.

Wang, Y. (2015). Frequencies of the Ricker wavelet. *Geophysics, 80,* 31–37.

Yin, W., Yin, X. Y., Wu, G. C., & Liang, K. (2006). The method of finite difference of high precision elastic wave equations in the frequency domain and wave-field simulation. *Chinese Journal of Geophysics, 49,* 561–568.

Yuan, S., Wang, S., Sun, W., Miao, L., & Li, Z. (2014). Perfectly matched layer on curvilinear grid for the second-order seismic acoustic wave equation. *Exploration Geophysics, 45,* 94–104.

Zeng, Y., He, J., & Liu, Q. (2001). The application of the perfectly matched layer in numerical modeling of wave propagation in poroelastic media. *Geophysics, 66,* 1258–1266.

Zeng, C., Xia, J., Miller, R., & Tsoflias, G. (2011). Application of the multiaxial perfectly matched layer (M-PML) to near-surface seismic modeling with Rayleigh waves. *Geophysics, 76,* T43–T52.

Zhao, J., Huang, X., Liu, W., Zhao, W., Song, J., Xiong, B., et al. (2017). 2.5-D frequency-domain viscoelastic wave modelling using finite-element method. *Geophysical Journal International, 211,* 164–187.